Supplementary Information for

Mutual Functionalization of Dinitrogen and Methane Mediated by Heteronuclear Metal Cluster Anions CoTaC₂⁻

Li-Hui Mou,[a,c,d] Yao Li,[b,c,d] Gong-Ping Wei,[a,c,d] Zi-Yu Li,[*,a,d] Qing-Yu Liu,[a,d] Hui Chen,[*,b,d] and Sheng-Gui He[*,a,c,d]

[a]State Key Laboratory for Structural Chemistry of Unstable and Stable Species, Institute of

Chemistry, Chinese Academy of Sciences, Beijing 100190, P. R. China

[b]CAS Key Laboratory of Photochemistry, Institute of Chemistry, Chinese Academy of Sciences, Beijing 100190,

P. R. China

[c]University of Chinese Academy of Sciences, Beijing 100049, P. R. China

[d]Beijing National Laboratory for Molecular Sciences and CAS Research/Education Center of

Excellence in Molecular Sciences, Beijing 100190, P. R. China

[*]Corresponding authors.

Emails: liziyu2010@iccas.ac.cn, chenh@iccas.ac.cn, and shengguihe@iccas.ac.cn.

Table of Contents

1. Methods

1.1 Experimental Methods

Mass spectrometry. The $CoTaC_2^-$ cluster anions were generated by laser ablation of a mixed metal disk target compressed with Co and Ta powders (molar ratio Co/Ta = 2:1) in the presence of 0.05% CD_4 seeded in a He carrier gas with a backing pressure of about 6 standard atmospheres. The reaction of $CoTaC_2^-$ with N_2 was studied by using a single ion trap apparatus.[1,2] The $CoTaC_2^-$ ions were mass-selected by a quadrupole mass filter (QMF) and then entered into a linear ion trap (LIT) reactor, in which they were confined and cooled by collisions with a pulse of He gas for about 1.2 ms and then interacted with a pulse of N_2 for about 4.8 ms. The reaction of $CoTaC_2N_2^-$ with CH_4 was studied by using a newly-developed double ion trap apparatus (Scheme S1), which was equipped with two QMFs and two LITs and can spatially separate the addition of reactant gases. The $CoTaC_2N_2^-$ ions were generated from the reaction of $CoTaC_2^-$ that was mass-selected by the first QMF (QMF1) with N_2 in the first LIT reactor (LIT1), and then mass-selected by the second QMF (QMF2) and cooled to interact with CH_4 in the second LIT reactor (LIT2). To confirm the assigned reaction channels, isotopic labeling experiments using $^{15}N_2$ in place of N_2 and using CD_4 in place of CH_4 were performed. The delay between cooling gas pulse and reactive gas pulse was 2 ms. It has been proved that the clusters had been thermalized to (or close to) room temperature before reactions in the previous works.[2,3] The cluster ions ejected from the LIT were detected by a reflectron time-of-flight mass spectrometer (TOF-MS).
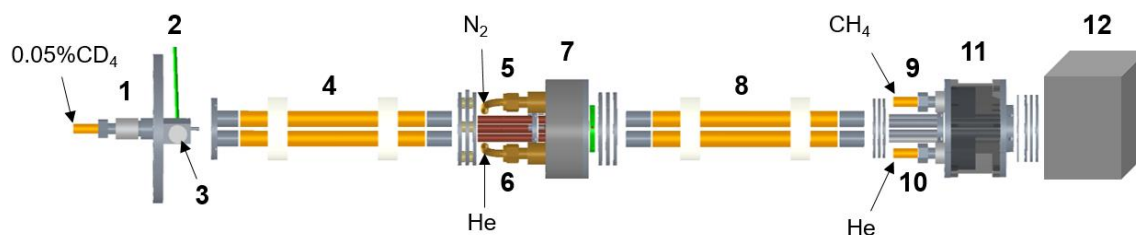
Scheme S1 A schematic diagram of the double ion trap apparatus. Labels 1−12: 1, 5, 6, 9 and 10 (pulsed valves), 2 (ablation laser, 532 nm), 3 (sample disk), 4 (the first quadrupole mass filter, QMF1), 7 (the first linear ion trap, LIT1), 8 (the second quadrupole mass filter, QMF2), 11 (the second linear ion trap, LIT2) and 12 (reflectron time-of-flight mass spectrometer, TOF-MS).

The reaction of $FeTaC_2^-$ with N_2 has been studied in a previous work,[4] while this work focuses on the reaction of the N≡N cleavage product $FeTaC_2N_2^-$ with CH_4, which might be very slow and was not detected by using the LIT reactor. We recently designed a ship-lock-type reactor (SLTR), which can work under high gas pressures up to 1000 Pa to detect slow ion-molecule reactions. The detailed description of the whole experimental apparatus was shown in a previous work.[5] The $FeTaC_2^-$ was generated by laser ablation of a mixed metal disk target compressed with Fe and Ta powders (molar ratio Fe/Ta = 2:1) in the presence of 0.02% CD_4 seeded in a He carrier gas. After that, the $FeTaC_2^-$ was mass-selected by the QMF and trapped by the SLTR to interact with He, N_2 or a mixed gas of N_2 and CH_4 at a gas pressure of 10~20 Pa for about 60 ms. After the reaction, the reactant and product ions were delivered into the reflectron TOF-MS for mass and abundance measurements.

Photoelectron imaging spectroscopy (PEIS). The PEIS characterization experiments of $CoTaC_2^-$ and $CoTaC_2N_2^-$ ions were carried out with a separate apparatus of tandem TOF-MS equipped with a laser ablation cluster source, a fast flow reactor, a linear ion trap and a photoelectron imaging spectrometer.[4,6] The $CoTaC_2^-$ ions were generated in the laser ablation cluster source according to the procedure mentioned above. The $CoTaC_2N_2^-$ ions were generated from the reaction of $CoTaC_2^-$ with N_2 in the linear ion trap. Changing reaction temperatures (170 K, 200 K, and 250 K) for the $CoTaC_2^-$/N_2 reaction system can bring about substantial changes on the spectra of $CoTaC_2N_2^-$, which is helpful to assign the structure of $CoTaC_2N_2^-$ and verify the reliability of theoretical calculations. Note that the residual water in the room-temperature ion trap will deplete the $CoTaC_2^-$ signal, so room-temperature reaction was not performed in the PEIS experiment. The reaction time was 60~80 ms to enable collisional quenching of vibrationally excited states. For the same reason, the $CoTaC_2^-$ ions were introduced into the ion trap that was held at 10 K and cooled with He for about 80 ms. For acquisition of PEIS spectra, the cooled reactant and product ions were extracted from the ion trap into the TOF-MS, and then mass-selected and photon-detached with a wavelength-tunable laser beam (pulse width of ~5 ns) delivered from an optical parametric oscillator laser source. The kinetic energies (or velocities) of the photon-detached electrons were measured by the photoelectron imaging spectrometer. The PEIS spectra were calibrated using the spectrum of Au^- taken at similar conditions. The resolution of the photoelectron imaging spectrometer was approximately 30 meV at electron kinetic energy of 1 eV.

1.2 Theoretical Methods

Density functional theory (DFT) calculations. All structures in this work were optimized at the DFT level using the Gaussian 09 program package.[7] The pure TPSS functional[8] was employed throughout this work given that it performs the best for the bond dissociation energies of several species containing Co, Ta, C and N atoms when compared with available experimental data (Supplementary Table 1). The polarized split-valence basis set 6-311+G(d) for C, N and H atoms, the polarized triple-ζ valence basis set Def2-TZVP for the Co atom, and the Def2-TZVP basis set combined with an effective core potential for the Ta atom were used in the DFT calculations.[9-11] The initial guess structures of intermediates (IMs) and transition states (TSs) were obtained through relaxed potential energy surface scans using the single or multiple internal coordinates.[12] Vibrational frequency calculations were performed to check that each of the IMs and TSs has zero and only one imaginary frequency, respectively. Intrinsic reaction coordinate (IRC) calculations were performed so that a TS connects two appropriate local minima.[13,14] The zero-point vibration corrected energies (ΔH_0, enthalpies at 0 K) in unit of eV are reported in this work. Natural bond orbital (NBO) analysis was performed using NBO 5.9 program implemented in Gaussian 09 and the Multiwfn program.[15,16]

High-level single-point energy calculations. To obtain reliable relative energies, the single-point energies of DFT-optimized structures were calculated by high-level RCCSD(T) (partially spin-adapted open-shell coupled cluster method with single, double, and perturbative triple excitations)[17-20] and DMRG-SC-NEVPT2 (density matrix renormalization group strongly-contract n-electron valance perturbation theory)[21,22] methods using Molpro, PySCF and BLOCK program packages.[23-30] In the RCCSD(T) calculations, all the valence electrons were correlated and the reference orbitals are based on the restricted open-shell Kohn-Sham (KS) orbitals of TPSS functional. The Hartree–Fock (HF) reference orbital was not adopted because (1) the KS orbital has included the electron correlation effect while the HF orbital does not, and (2) using DFT method can avoid the convergence problem in the HF method for first-row transition metals.[31,32] Note that the multi-configurational character of most of the calculated species is not serious and the T_1 diagnostic values in RCCSD(T) calculations are below 0.05 (Supplementary Table 2), which means that the RCCSD(T) results are reliable. However, isomers ^{2}IS2 and ^{2}IS6 have obvious multi-configurational character (with three unpaired electrons), it is not possible to get the proper restricted open-shell single reference required for reliable RCCSD(T) calculations. Therefore, the DMRG-SC-NEVPT2 method based on the DMRG reference was used to obtain their energies relative to the corresponding quartet state isomers (^{2}IS2 vs ^{4}IS2, ^{2}IS6

vs ^{4}IS6), and their energies relative to the lowest-lying isomer ^{2}IS1 were obtained through the RCCSD(T) results of ^{4}IS2/^{4}IS6. An active space of (21 o, 23 e) containing five Co 3d, one Co 4s, one Co 4d, five Ta 5d, one Ta 6s, two C 2s, and six C 2p orbitals was used for ^{2,4}IS6, while a smaller active space of (20 o, 23 e) without the Co 4d orbital was used for ^{2,4}IS2 in the DMRG-CASSCF (density matrix renormalization group complete active space self-consistent field) calculations. The additional Co 4d orbital in the active space (21 o, 23 e) used for IS6 is caused by the fact that in this case, the doubly occupied 3d orbital of Co cannot be retained in the active space without the corresponding 4d orbital. The DFT natural orbitals were selected as initial orbitals and further optimized in DMRG-CASSCF ($M = 500$, no frozen core) calculations. From the DMRG-CASSCF optimized orbitals, the larger DMRG-CI (density matrix renormalization group configuration interaction) calculations with $M = 2000$ and $M = 3000$ were carried out to check if the results converged. It turned out that the energy was only improved by 0.5 mEh from $M = 2000$ to $M = 3000$, which indicates that $M = 2000$ is enough for convergence. The same M value was also used in the subsequent DMRG-SC-NEVPT2 calculations. Two augmented correlation consistent basis sets of aug-cc-pVDZ/aug-cc-pVDZ-PP (AVDZ) and aug-cc-pVTZ/aug-cc-pVTZ-PP (AVTZ) were used for Co, C, N, H, and Ta atoms, in which the Stuttgart relativistic energy-consistent small-core pseudopotential (PP) was adsorbed for the Ta atom for an approximate treatment of relativistic effects.[33-36] The two-point complete basis set (CBS) limit extrapolation from AVDZ and AVTZ data was conducted by using the Helgaker's two-point CBS limit extrapolation scheme,[37-39] with total correlation energy extrapolated with the equation $E_{corr,n} = E_{corr,CBS} + A/n^3$. The reference energy CBS limit (Hartree–Fock energy) was not obtained from extrapolation but was approximated by the AVTZ-calculated reference energy. The reported energies at the RCCSD(T) level are zero-point-vibration corrected, in which the electronic energies are from RCCSD(T) calculations and the zero-point corrections are from frequency calculations by the DFT method.

Theoretical simulations of photoelectron spectra. The Frank-Condon (FC) simulations of photoelectron spectra for CoTaC$_2^-$ were performed with the program ezSpectrum based on the double-harmonic approximation.[40] The simulation temperature was set to 10 K to fit the PEIS experiment of CoTaC$_2^-$. The required geometric structures, vibrational modes, and harmonic frequencies were from DFT calculations and the adiabatic electron detachment energies (ADEs) were from RCCSD(T) calculations. Each vibrational transition peak is fitted by a unit-area Gaussian function with the full width at half maximum (FWHM) of 6 meV.[41] The density of state (DOS)

simulations of photoelectron spectra for $CoTaC_2N_2^-$ were performed with the Multiwfn program based on the generalized Koopmans' theorem.[42] The required molecular orbital energies were from DFT calculations and the vertical electron detachment energies (VDEs) were form RCCSD(T) calculations. The simulated spectra were obtained by fitting the distribution of the transition lines by the unit-area Gaussian functions with the FWHM of 0.15 eV.

RRKM-based calculations. The Rice-Ramsperger-Kassel-Marcus (RRKM) theory and RRKM-based variational transition state theory (VTST)[43] were used to calculate the forward conversion rates (k_t) of traversing TSs from IMs and the H_2 desorption rates (k_d). For these calculations, the energy (E) of the reaction intermediate and the energy barrier ($E^\ddagger$) for each step were needed. The E values of IMs are defined as the following equation:

$$E(\text{IMs}) = E_{vib}(\text{cluster}) + E_{vib}(\text{molecule}) + E_k + E_b$$

in which E_{vib} represents the vibrational energy taken from DFT calculations, E_k represents the center of mass kinetic energy calculated by $E_k = \mu v^2/2$ (μ is the reduced mass and v is the velocity), and E_b represents the binding energy taken from RCCSD(T) calculations.

The rate constants $k(E)$ were calculated by the following Equation:

$$k(E) = gN^{\neq}(E - E^{\neq})/\rho(E)/h$$

in which g is the symmetry factor (g is taken as 1), $\rho(E)$ denotes the density of states of IMs at the energy of E, $N^{\neq}(E - E^{\neq})$ is the total number of the states of TSs with a barrier of $E^{\neq}$ ($E^{\neq}$ was taken from RCCSD(T) calculations), and h is the Planck constant. The $\rho(E)$ and $N^{\neq}(E - E^{\neq})$ were obtained by the direct count method[44] with the DFT-calculated vibrational frequencies under the approximation of harmonic vibrations.

Considering that no distinct TS exists on the potential energy surfaces for H_2 desorption, VTST calculations were performed through geometry optimizations of adsorption complexes by moving the H_2 unit away from the cluster (maximal distance of 5 Å). The $k(E)$ value of each step was estimated and the minimum rate was considered as the k_d value.

The collision rate (k_{col})[45] that a cluster experiences with the buffer gas in the ion trap reactor is calculated by the following Equation:

$$k_{col} = 2\pi(e^2\alpha/\mu)^{1/2} \times N$$

in which e is the charge of the cluster ion, α is the electric polarizability of He, μ is the reduced mass, and N is the molecular density of He.

2. Additional studies on cluster reactivity and structural characterization

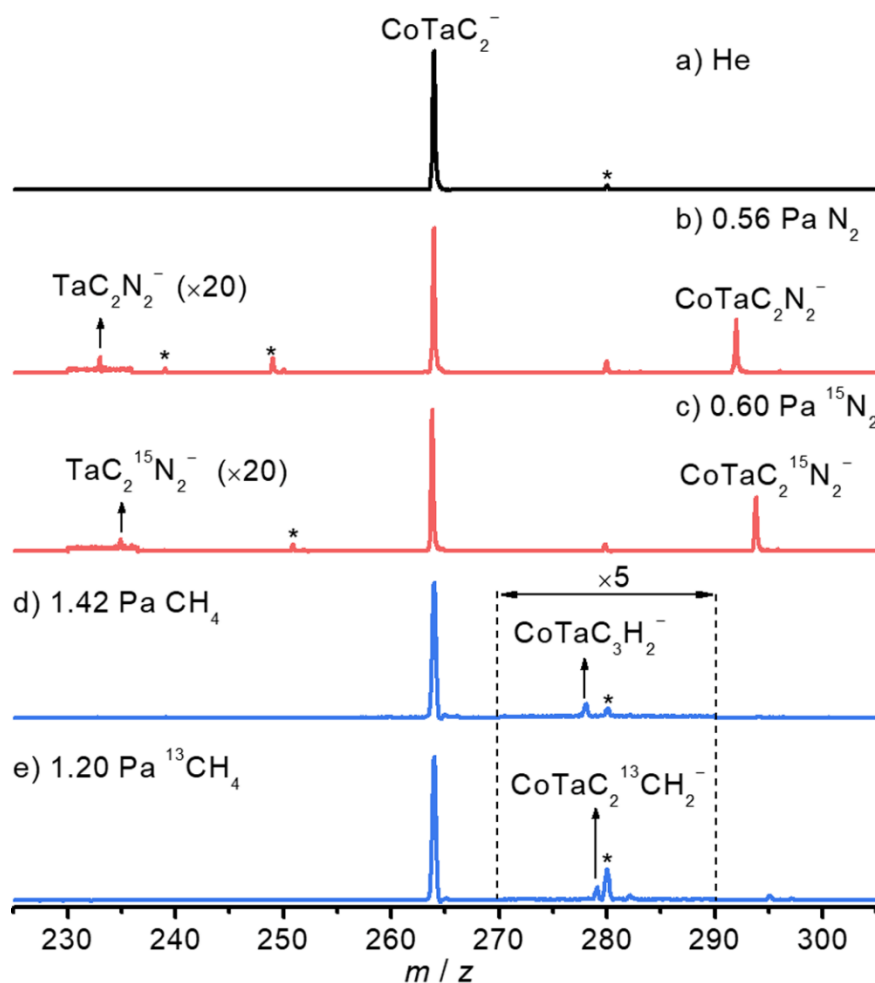### 2.1 Mass spectra for the reactions of $CoTaC_2^-$ with N_2 and CH_4

Fig. S1 TOF mass spectra for the reactions of mass-selected $CoTaC_2^-$ with (a) He, (b) N_2, (c) $^{15}N_2$, (d) CH_4 and (e) $^{13}CH_4$ for about 4.8 ms. Peaks marked with asterisks are due to water impurities in the gas handling system.

As shown in Fig. S1b and c, the adsorption of N_2 on $CoTaC_2^-$ ($CoTaC_2^- + N_2 \rightarrow CoTaC_2N_2^-$) is the major reaction channel upon the interaction of $CoTaC_2^-$ with N_2, and a very tiny metal atom ejection channel ($CoTaC_2^- + N_2 \rightarrow TaC_2N_2^- + Co$) was also observed. When the $CoTaC_2^-$ reacts with CH_4 and $^{13}CH_4$ (Fig. S1d and e), a weak product peak assigned as $CoTaC_3H_2^-$ and $CoTaC_2^{13}CH_2^-$ appeared, suggesting the elimination of a H_2 molecule ($CoTaC_2^- + CH_4 \rightarrow CoTaC_3H_2^- + H_2$). The rate constant of this pseudo-first-order reaction was estimated to be $(1.2 \pm 0.2) \times 10^{-14}$ cm^3 molecule^{-1} s^{-1}, which is 3 orders of magnitude slower than the reaction of $CoTaC_2N_2^-$ with CH_4.

2.2 Reaction kinetics for the CoTaC₂⁻/N₂, CoTaC₂N₂⁻/CH₄, and CoTaC₂N₂⁻/CD₄ reaction systems
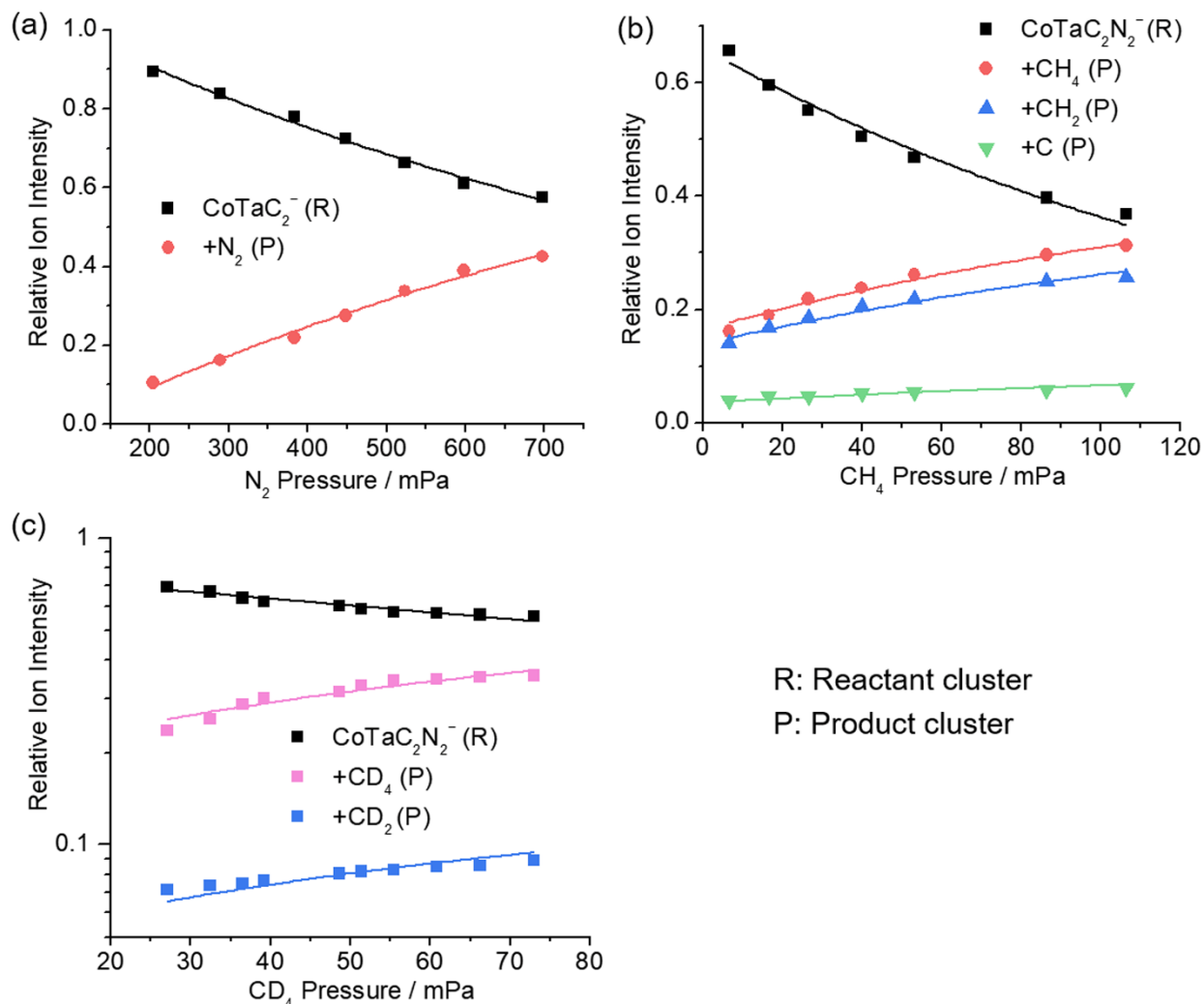

Fig. S2 Variation of relative intensities of reactant and product ions with respect to the reactant gas effective pressures in the reactions of (a) CoTaC$_2^-$ with N$_2$, (b) CoTaC$_2$N$_2^-$ with CH$_4$, and (c) CoTaC$_2$N$_2^-$ with CD$_4$. The solid lines are fitted to experimental data points with the approximation of the pseudo-first-order reaction mechanism.

The rate constants (k_1) of the pseudo-first-order reactions of CoTaC$_2^-$ with N$_2$, CoTaC$_2$N$_2^-$ with CH$_4$, and CoTaC$_2$N$_2^-$ with CD$_4$ were estimated by a least-squares fitting procedure on the basis of equation (1).[46] In equation (1), the I_R is the intensity of the reactant cluster ions after the reaction, I_T is the total ion intensity after the reaction, P is the effective pressure of the reactant gas, k_B is the Boltzmann constant, T is the temperature (298 ± 3 K) of the reactant gas, and t_R is the reaction time. The effective pressure of the reactant gas P is determined by equation (2), where P_{max} is the instantaneous gas pressure in the ion trap when the pulsed valve is closed, τ_R and δt_R are the decay time and pulse width for reactant gas, respectively. The P_{max} is determined by equation (3), where N is the number of

molecules injected into the ion trap within the pulse width of δt_R, V is the volume of the ion trap (4.9×10^4 mm^3). More details of the definition of effective pressure can be found in a previous work.[2]

$$\ln \frac{I_R}{I_T} = -k_1 \frac{P}{k_B T} t_R \tag{1}$$

$$P \equiv P_{max} \frac{\tau_R}{t_R} \left[1 + \frac{\delta t_R}{2\tau_R} - e^{-(t_R - \delta t_R)/\tau_R} \right] \tag{2}$$

$$P_{max} = \frac{N k_B T}{V} \frac{\tau_R}{\delta t_R} \left(1 - e^{-\delta t_R / \tau_R} \right) \approx \frac{N k_B T}{V} \tag{3}$$

the systematic deviations of t_R ($\pm 3\%$), T ($\pm 2\%$), and P ($\pm 20\%$) and the standard error in the least-squares fitting procedure were considered to estimate the uncertainties of the rate constants.
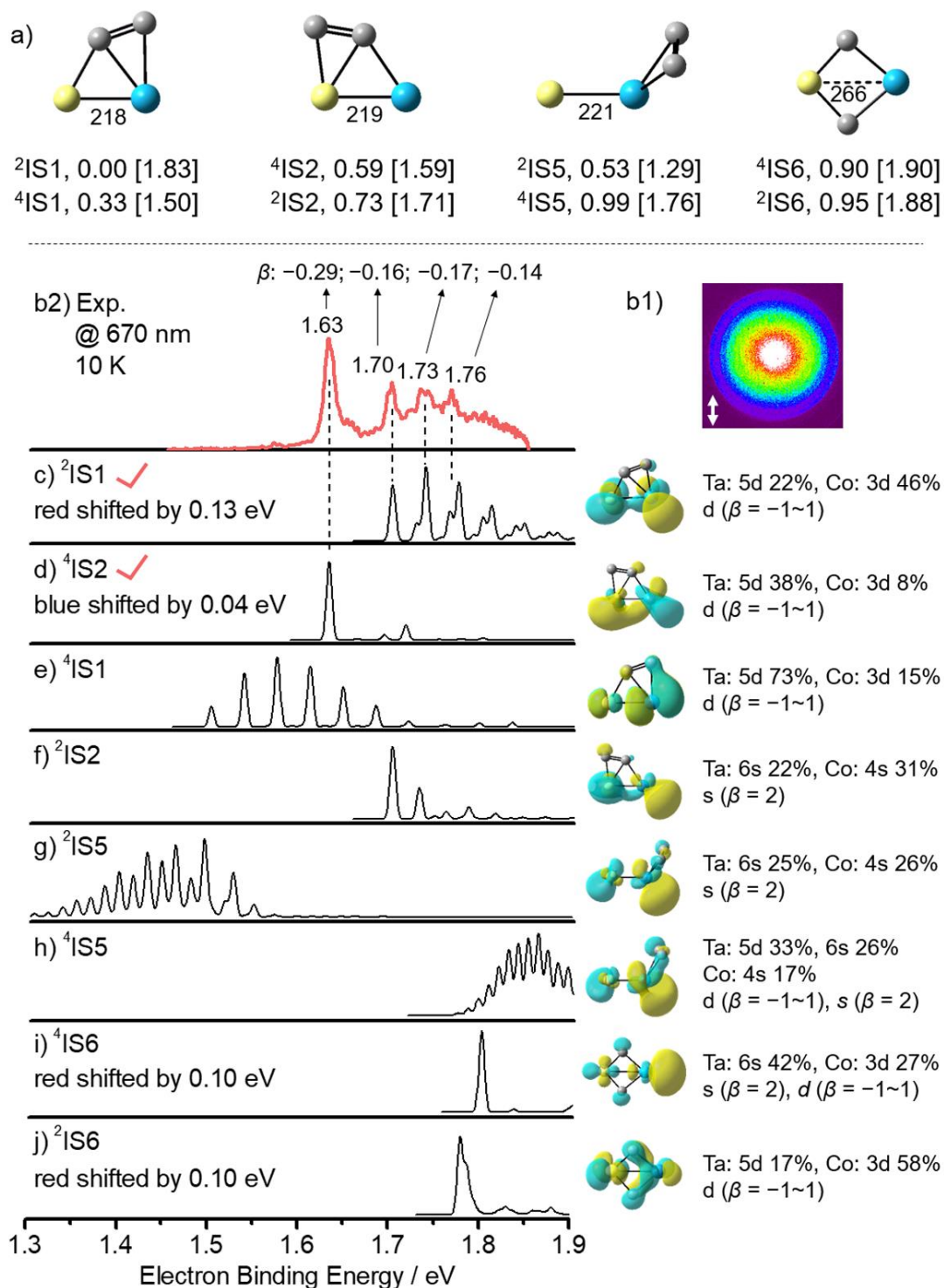
2.3 Structural characterization of CoTaC$_2^-$

Fig. S3 (a) DFT optimized low-lying isomers of CoTaC$_2^-$. The relative energies and ADEs (in square brackets) in unit of eV are calculated at the RCCSD(T)/DMRG-SC-NEVPT2 levels. (b) Raw photoelectron image and the transformed photoelectron spectrum of CoTaC$_2^-$ recorded with 670 nm photons at 10 K. The double-headed arrow indicates the laser polarization. The anisotropy parameters (β) of the four peaks are shown. (c-j) FC-simulated photoelectron spectra of the low-lying isomers. The highest occupied molecular orbitals (HOMOs) and their major orbital components are given. The corresponding β values resulted from electron detachment from s, p and d atomic orbitals are shown.

The experimental photoelectron spectrum of $CoTaC_2^-$ taken with 670 nm photons at 10 K (Fig. S3b) has four major peaks centered at 1.63, 1.70, 1.73 and 1.76 eV. The anisotropy parameters (β) can be obtained from the experimental spectrum and quantify the degree of alignment between the direction of photo-detached electrons and the laser polarization.[6] To satisfy the dipole selection rule, $\Delta l = \pm 1$, the electron detachment from s ($l = 0$) atomic orbital generate one type (s $\rightarrow$ p, $l = 0 + 1$) of outgoing partial wave with maximum intensity parallel to the laser polarization direction and $\beta = 2$. The electron detachment from p and d atomic orbitals can generate two types (p $\rightarrow$ s/d; and d $\rightarrow$ p/f) of outgoing partial waves and their pure interference can result in $\beta = -1$. Without interferences, the p $\rightarrow$ s, p $\rightarrow$ d, d $\rightarrow$ p, and d $\rightarrow$ f partial waves have the β parameters ranging from 0 to 1. The β values of the four peaks were estimated to be −0.29, −0.16, −0.17 and −0.14. The obvious difference in β values between the first peak and the following three peaks indicates that they are likely to come from two different electronic states. The FC-simulated spectrum of the $^2A \rightarrow {}^3A$ vibrational transition for the lowest-lying isomer $^2IS1$ can reasonably reproduce the experimental spectrum from 1.70 to 1.76 eV (Fig. S3c), and the calculated ADE (1.83 eV) of $^2IS1$ is close to the experimental value of 1.70 eV. Therefore, the $^2IS1$ is the most probable species of $CoTaC_2^-$ generated in the cluster source. The first peak centered at 1.63 eV may be contributed by the isomer $^4IS2$ with relative energy of 0.59 eV higher than $^2IS1$, because the $^4IS2$ has the matched spectral profile and VDE value (1.59 eV vs 1.63 eV) compared to the first peak (Fig. S3d). Note that the integration intensity (peak area) of the band covering peaks at 1.70, 1.73, and 1.76 eV is about 2.6 times larger than that of the first peak, which is consistent with the conclusion that $^2IS1$ is the most probable species of $CoTaC_2^-$ while $^4IS2$ takes minor population. Besides, the HOMOs of $^2IS1$ and $^4IS2$ are mainly composed of Ta 5d and Co 3d orbitals, which agrees with the β parameters of the experimental spectrum close to 0. The high-energy environment in the laser ablation cluster source can enable the formation of $CoTaC_2^-$ clusters with different energies,[47,48] which were subsequently cooled to their ground electronic states, such as $^4IS1 \rightarrow {}^2IS1$ and $^2IS2 \rightarrow {}^4IS2$, so the higher isomers $^4IS1$ and $^2IS2$ could be excluded (Fig. S3e and f). The isomers $^{2,4}IS5$ have obviously no contribution to the spectrum of $CoTaC_2^-$ because of their mismatched DOS simulations compared with the experimental spectrum (Fig. S3g and h). The isomers $^{2,4}IS6$ are also unlikely to exist due to their very high energies (> 0.90 eV) and greatly deviated ADE values compared to the experiment (Fig. S3i and j).

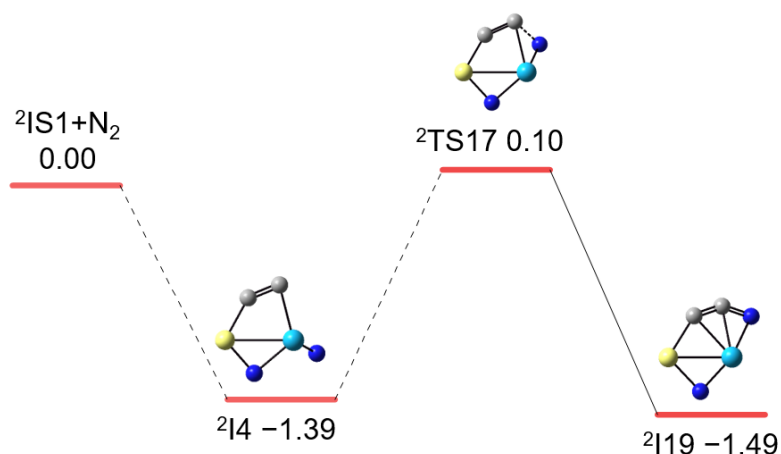## 2.4 Additional reaction pathways for CoTaC$_2^-$ with N$_2$

Fig. S4 RCCSD(T)-calculated kinetically unfavorable N–C$_{cluster}$ coupling process in the reaction of the lowest-lying isomer (^{2}IS1) of CoTaC$_2^-$ with N$_2$. The zero-point vibration corrected energies with respect to ^{2}IS1 + N$_2$ are given in eV.

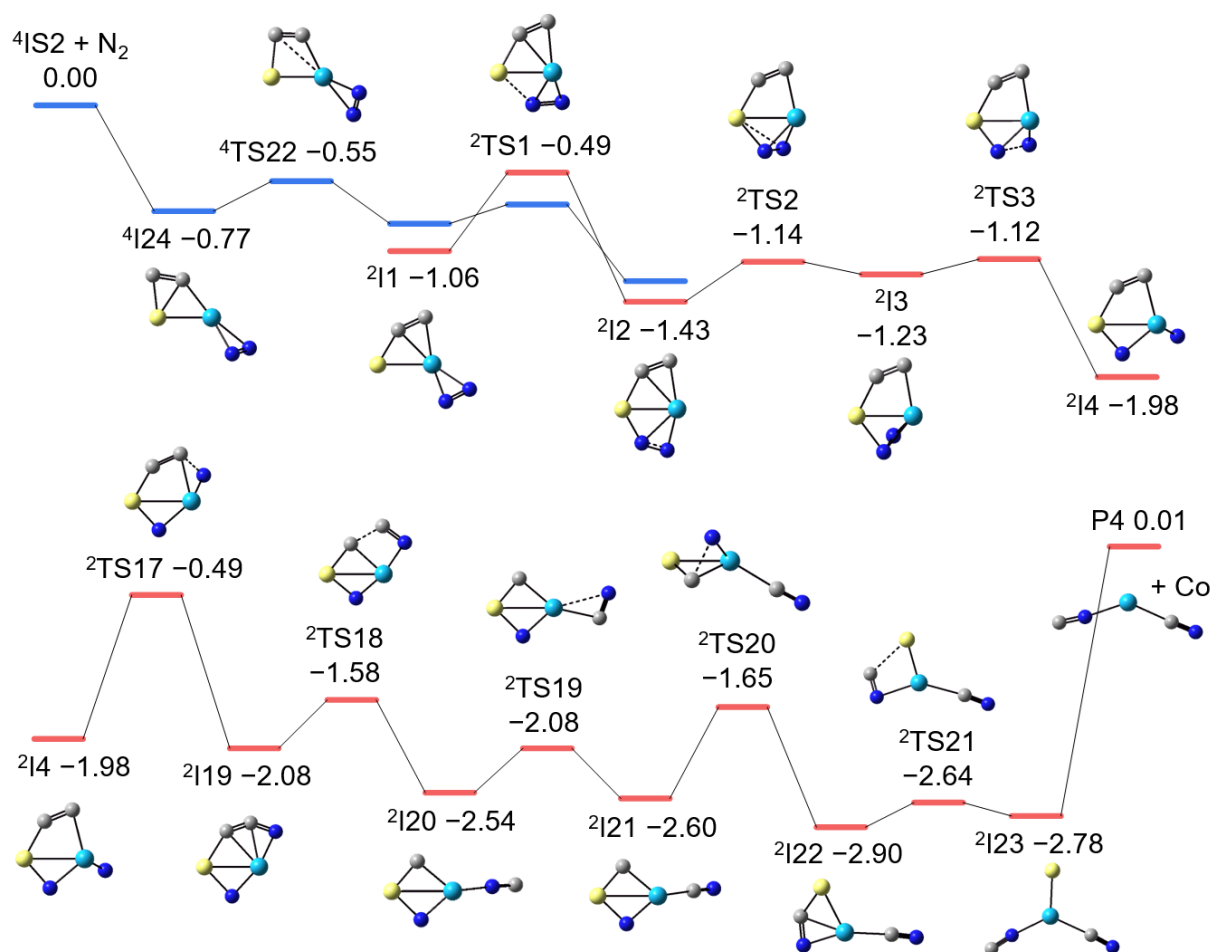**Fig. S5** RCCSD(T)-calculated potential energy profile for the production of TaC$_2$N$_2^-$ + Co from CoTaC$_2^-$ (^{4}IS2) + N$_2$. The zero-point vibration corrected energies with respect to ^{4}IS2 + N$_2$ are given in eV.

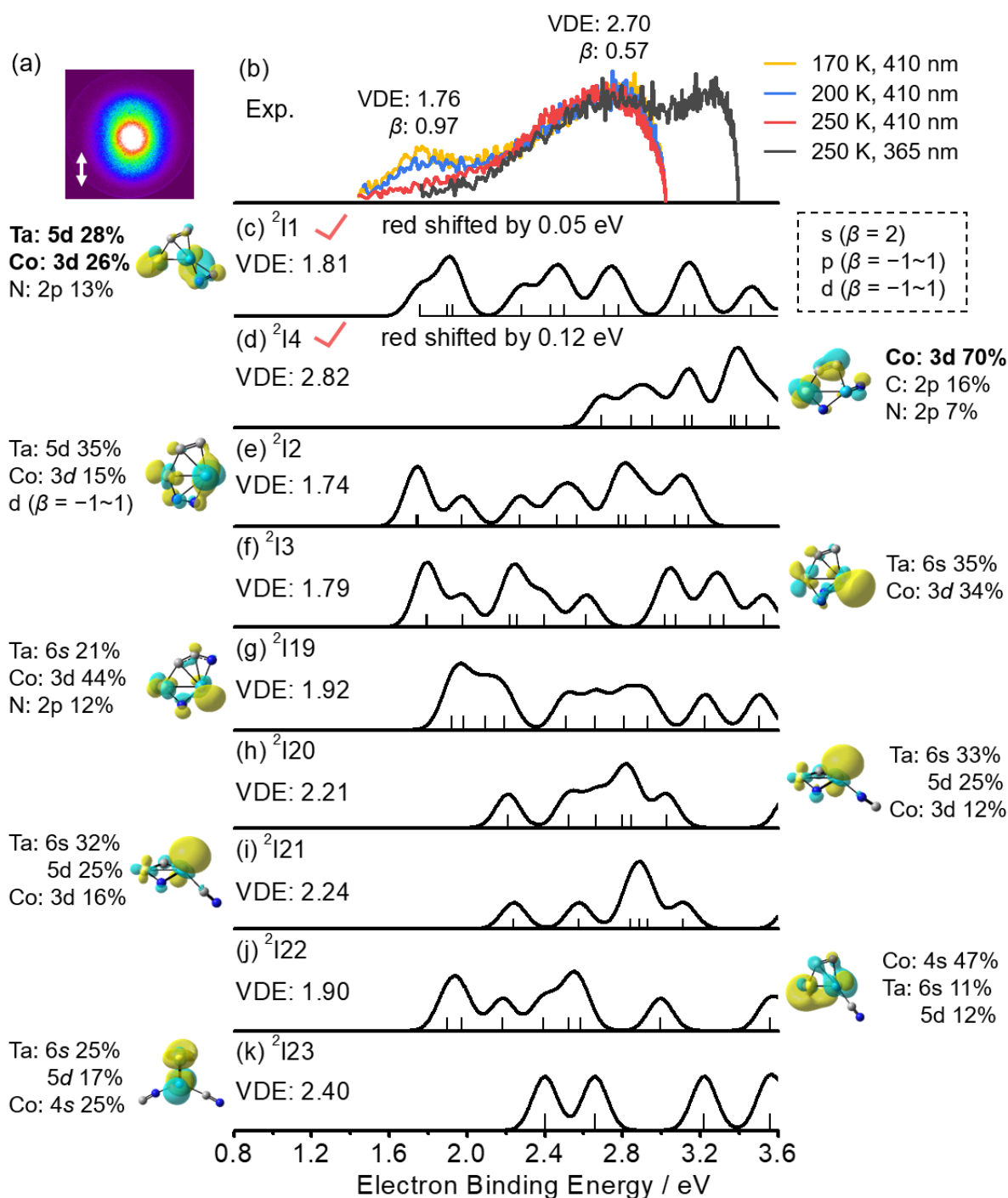## 2.5 Structural characterization of $CoTaC_2N_2^-$

Fig. S6 (a) Raw photoelectron image recorded with 365 nm photons at 250 K. The double-headed arrow indicates the laser polarization. (b) The experimental photoelectron spectra of $CoTaC_2N_2^-$ recorded at different reaction temperatures and photon energies. The anisotropy parameters (β) of the first two peaks are shown. (c-k) DOS-simulated photoelectron spectra of intermediates $^2I1–^2I4$ and $^2I19–^2I23$. The HOMOs and their major orbital components for each intermediate are given. The corresponding β values resulted from electron detachment from s, p and d atomic orbitals are shown.

The photoelectron spectrum of $CoTaC_2N_2^-$ recorded with 365 nm photons at 250 K revealed that the VDE is about 2.70 eV (Fig. S6b). The DOS-simulated spectrum of $^2I4$ and its RCCSD(T)

calculated VDE (2.82 eV) can reasonably reproduce those of the experimental spectrum (Fig. S6d). Moreover, the β value of the first peak of 365 nm spectrum is estimated to be 0.57, which indicates that the electron detachment occurs in a p or d atomic orbital. This agrees with the fact that the HOMO of ^{2}I4 is mainly composed of Co 3d orbital. Therefore, the ^{2}I4 is the most probable species of $CoTaC_2N_2^-$ generated at 250 K and room temperature (298 K). Interestingly, compared with the 250 K spectrum of $CoTaC_2N_2^-$, an additional peak centered at 1.76 eV appeared in the spectra recorded at 200 K and 170 K, suggesting the stabilization of an additional intermediate due to the presence of a temperature-sensitive transformation step. The reaction pathway of $CoTaC_2^- + N_2$ calculated at the RCCSD(T) level showed that the rate-limiting step of ^{2}I1 → ^{4}TS1 → ^{2}I2 involves a spin inversion and a high TS (^{4}TS1/−0.13 eV), which indicates that the ^{2}I1 is the most probable species that could be stabilized at lower temperatures. In contrast, the ^{2}I2 and ^{2}I3 have no chance to be stabilized due to the low energy barriers for their forward transformation. Indeed, the calculated VDE (1.81 eV) of ^{2}I1 is close to the experimental value of 1.76 eV, and its DOS-simulated spectrum can well reproduce the first spectral peak (Fig. S6c). Moreover, the HOMO of ^{2}I1 is mainly composed of Ta 5d and Co 3d orbitals, which can interpret the β value of 0.97 in the experiment. Such temperature-dependent spectra of $CoTaC_2N_2^-$ verified the reliability of our RCCSD(T) calculations in predicting the reaction kinetics of $CoTaC_2^-/N_2$ reaction system. Following this conclusion, one can understand that due to the high positive energy barrier for the further transformation of ^{2}I4 (Fig. S4), the ^{2}I4 would be stabilized as the adsorption product $CoTaC_2N_2^-$ at room temperature. The intermediates ^{2}I19–^{2}I23 with CN units have mismatched VDE values (1.90~2.40 eV) and/or spectral profiles (Fig. S6g-k) compared with the experimental spectrum and can be excluded to have contribution to the 250 K spectrum. Test calculations on the activation of CH_4 by all $CoTaC_2N_2^-$ isomers (Fig. S7) further support the identification of ^{2}I4 as the adsorption product at room temperature.
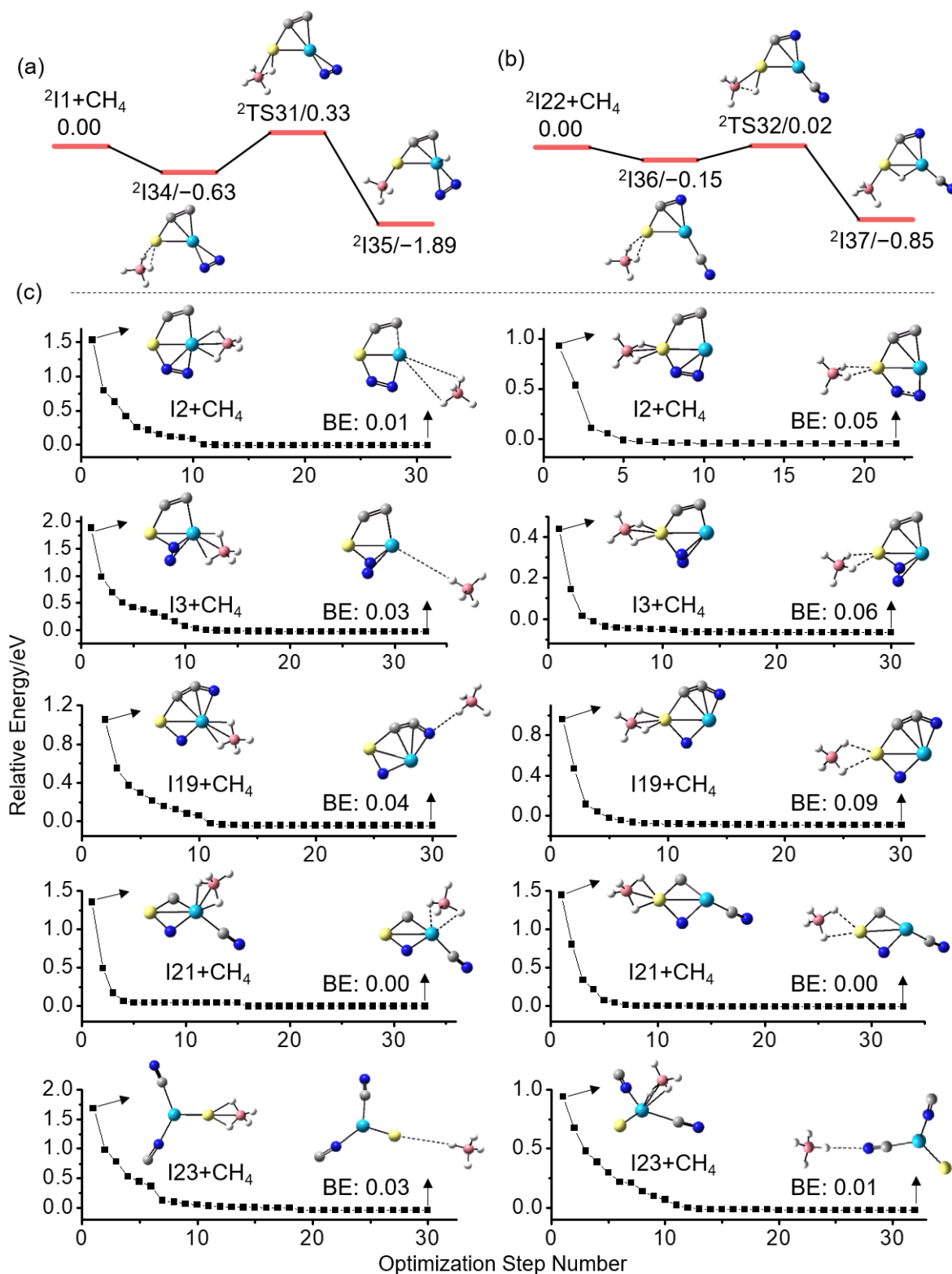
Fig. S7 RCCSD(T)-calculated potential energy profiles for the interaction of $CoTaC_2N_2^-$ isomers $^2I1$ (a) and $^2I22$ (b) with CH_4. (c) DFT-calculated adsorption of CH_4 on other $CoTaC_2N_2^-$ isomers along the reaction pathway. The binding energies (BE) relative to corresponding separated reactants ($CoTaC_2N_2^- + CH_4$) are given. The high energy barriers in (a, b) and small BE values in (c) indicate that these intermediates cannot react with CH_4.

In this study, CH_4 can serve as a probe molecule to characterize the structure of $CoTaC_2N_2^-$ because mass spectrometry experiments have showed that the $CoTaC_2N_2^-$ can react with CH_4 to produce $CoTaC_2N_2CH_{4,2,0}^-$ ions. The generation of $CoTaC_2N_2CH_{4,2,0}^-$ from the reaction of $^2I4$ with CH_4 has been demonstrated to be kinetically favorable in the main text. The reactions of other $CoTaC_2N_2^-$ isomers ($^2I1$–$^2I3$ and $^2I19$–$^2I23$) with CH_4 were also theoretically tested. As shown in Fig. S7c, most of them cannot trap CH_4 in the initial interaction due to the very small binding energies (< 0.10 eV). Although the $^2I1$ can initially bind CH_4 with a relatively larger binding energy of 0.63 eV (Fig. S7a), activation of the first C–H bond would be impeded by a high positive energy barrier ($^2TS31$/0.33 eV). For the reaction pathway of $^2I22$ with CH_4, the TS ($^2TS32$/0.02 eV) for activating the first C–H bond is slightly higher than the reaction entrance and is kinetically unfavorable (Fig. S7b), which disagrees with the rapid reaction rate (1.4 × 10^{-11} cm^3 molecule^{-1} s^{-1}) between $CoTaC_2N_2^-$ with CH_4. In contrast, the $^2I4$ can bind CH_4 with a large binding energy of 0.44 eV and the energy barrier for the first C–H cleavage is easily surmountable as it is 0.26 eV lower in energy with respect to the entrance channel. These results indicate that the $^2I4$ with a terminal N atom should be identified as the species of $CoTaC_2N_2^-$ generated from the room-temperature reaction of $CoTaC_2^-$ with N_2.

3. Additional theoretical analysis

3.1 Evidence of the reliability of theoretical methods

Supplementary Table 1 Experimental and calculated bond dissociation energies [D_0 (A–B) at 0 K, given in eV] of some species containing Co, Ta, C, and N atoms. The standard deviation (σ) of calculated values with respect to experimental data is given.
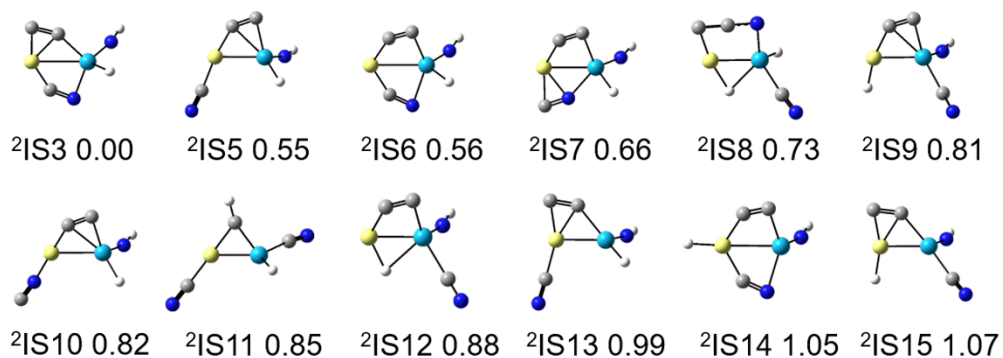
		D_0 (A–B) / eV	
		Co–C	Ta$^+$–C	Ta–N	N–N	C–N	C–C	
	Exp.[49,50]	3.90	3.79	6.25	9.75	7.77	6.37	σ
	TPSS	4.03	4.58	6.61	9.53	7.66	6.20	**0.068**
	M06L	3.95	5.12	6.47	9.41	7.75	6.34	0.106
	BPW91	4.80	4.71	6.96	9.95	8.05	6.50	0.121
Pure	BLYP	4.63	4.79	6.85	10.09	8.04	6.35	0.124
	BPBE	4.81	4.77	6.97	9.95	8.05	6.51	0.124
	BP86	4.95	5.19	6.97	10.25	8.25	6.61	0.160
	PBEPBE	4.99	5.19	7.19	10.24	8.31	6.72	0.210
	B3PW91	3.32	4.44	6.33	9.65	7.49	6.08	0.091
	B3LYP	3.28	4.53	6.34	9.60	7.51	6.06	0.106
	PBE1PBE	3.01	4.43	6.26	9.43	7.48	6.10	0.128
Hybrid	B1B95	3.10	4.33	6.34	9.44	7.42	6.04	0.135
	B3P86	3.54	4.69	6.54	9.78	7.74	6.27	0.136
	B1LYP	2.71	4.30	6.04	9.33	7.25	5.80	0.164
	M062X	1.35	4.67	5.72	9.44	7.38	5.95	0.350

Supplementary Table 2 T_1 diagnostic values of the species involved in the reaction of $CoTaC_2^-+N_2$ and $CoTaC_2N_2^-+CH_4$ at the RCCSD(T)/AVTZ level.

Species for $CoTaC_2^-/N_2$ couple		T_1	Species for $CoTaC_2N_2^-/CH_4$ couple	T_1
	$^2IS1$	0.033	CH_4	0.008
	$^4IS1$	0.032	$^2I5$	0.027
	$^2IS2$	-	$^2TS4$	0.027
	$^4IS2$	0.027	$^2I6$	0.027
$CoTaC_2^-$	$^2IS5$	0.037	$^2TS5$	0.027
	$^4IS5$	0.042	$^2I7$	0.039
	$^2IS6$	-	$^2TS6$	0.028
	$^4IS6$	0.032	$^2I8$	0.024
N_2		0.008	$^2TS7$	0.025
$^2I1$		0.039	$^2I9$	0.024
$^4I1$		0.035	$^2TS8$	0.022
$^2TS1$		0.037	$^2I10$	0.023
$^4TS1$		0.036	$^2TS9$	0.023
$^2I2$		0.024	$^2I11$	0.021
$^4I2$		0.026	$^2TS10$	0.023
$^2TS2$		0.032	$^2I12$	0.021
$^2I3$		0.025	$^2TS11$	0.022
$^2TS3$		0.037	$^2I13$	0.022
$^2I4$		0.031	$CoTaC_2N_2CH_2^-$ ($^2IS3$)	0.023
$^2TS17$		0.026	$^2TS12$	0.026
$^2I19$		0.027	$^2I14$	0.025
$^2TS18$		0.022	$^2TS13$	0.024
$^2I20$		0.027	$^2I15$	0.022
$^2TS19$		0.028	$^2TS14$	0.026
$^2I21$		0.024	$^2I16$	0.026
$^2TS20$		0.024	$^2TS15$	0.024
$^2I22$		0.024	$^2I17$	0.029
$^2TS21$		0.033	$^2TS16$	0.028
$^2I23$		0.028	$^2I18$	0.031
			$CoTaC_2N_2C^-$ ($^2IS4$)	0.032
			H_2	0.006

3.2 Low-lying isomers of $CoTaC_2N_2CH_{2,0}^-$ and RRKM theory calculations

(a) $CoTaC_2N_2CH_2^-$

^{2}IS3 0.00 ^{2}IS5 0.55 ^{2}IS6 0.56 ^{2}IS7 0.66 ^{2}IS8 0.73 ^{2}IS9 0.81

^{2}IS10 0.82 ^{2}IS11 0.85 ^{2}IS12 0.88 ^{2}IS13 0.99 ^{2}IS14 1.05 ^{2}IS15 1.07

(b) $CoTaC_2N_2C^-$

^{2}IS4 0.00 ^{2}IS16 0.04 ^{2}IS17 0.17 ^{2}IS18 0.18 ^{2}IS19 0.40 ^{2}IS20 0.42

^{2}IS21 0.43 ^{2}IS22 0.54 ^{2}IS23 0.69 ^{2}IS24 1.24
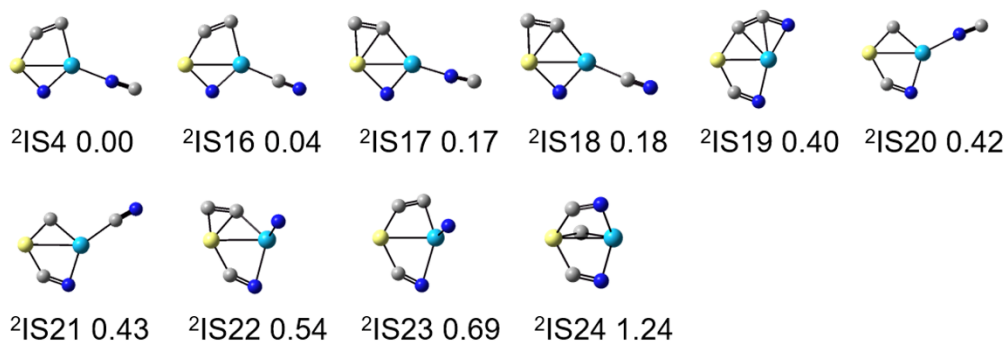
Fig. S8 DFT-calculated structures and relative energies for (a) $CoTaC_2N_2CH_2^-$ and (b) $CoTaC_2N_2C^-$. The energies are zero-point vibration corrected and in unit of eV. The superscripts indicate spin multiplicities.

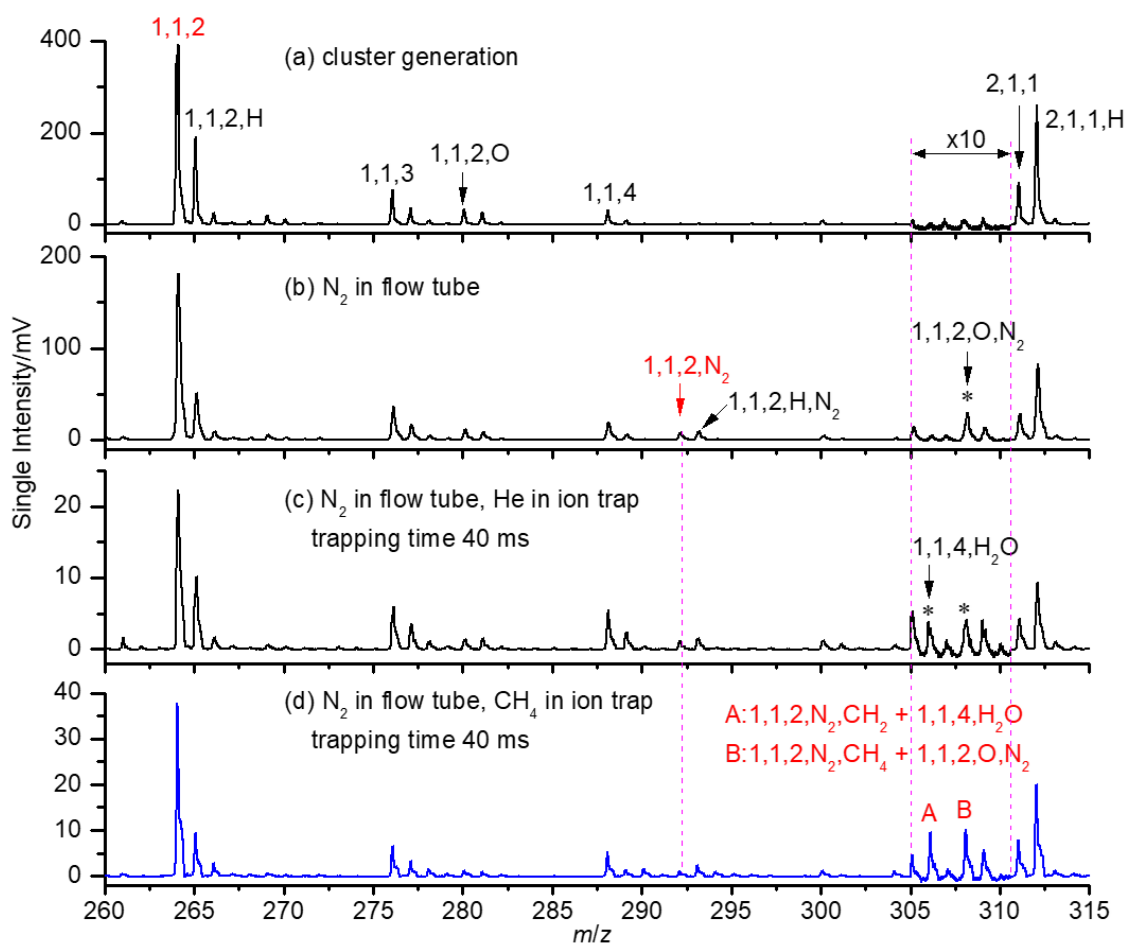**Fig. S9** Time-of-flight mass spectra for (a) the generation of $Co_xTa_yC_z^-$ (denoted as *x, y, z*) cluster anions, (b) the reactions of $Co_xTa_yC_z^-$ with N_2 in a flow tube reactor, (c) the reactions of $Co_xTa_yC_zN_2^-$ with He in an ion trap, and the reactions of $Co_xTa_yC_zN_2^-$ with CH_4 in the ion trap.

Supplementary Table 3 RRKM theory-calculated forward conversion rates (k_t) and H_2 desorption rates (k_d) in the reaction of $CoTaC_2N_2^-$ with CH_4. The collision rate between $(CoTaC_2N_2CH_4^-)^*$ and buffer gas He (2 Pa) at 298 K is given.

Reaction process	k_t (s^{-1})	k_{col} (s^{-1})
I5 → TS4	2.7×10^{10}	
I6 (P1) → TS5	6.9×10^4	
I6 (P1) → TS5[a]	3.3×10^5	
I6 → TS6	5.6×10^8	
I6 → TS7	7.5×10^{11}	6.7×10^5
I9 → TS8	3.3×10^{11}	
I9 → TS9	4.9×10^9	
I9 → TS10	2.0×10^{11}	
I9 → TS11	1.2×10^{13}	

	k_d (s^{-1})	
I13 → P2 (^{2}IS3 + H_2)	6.9×10^{11}	

[a]RRKM theory-calculated rate in the case that the barrier height of TS5 is decreased by 0.1 eV.

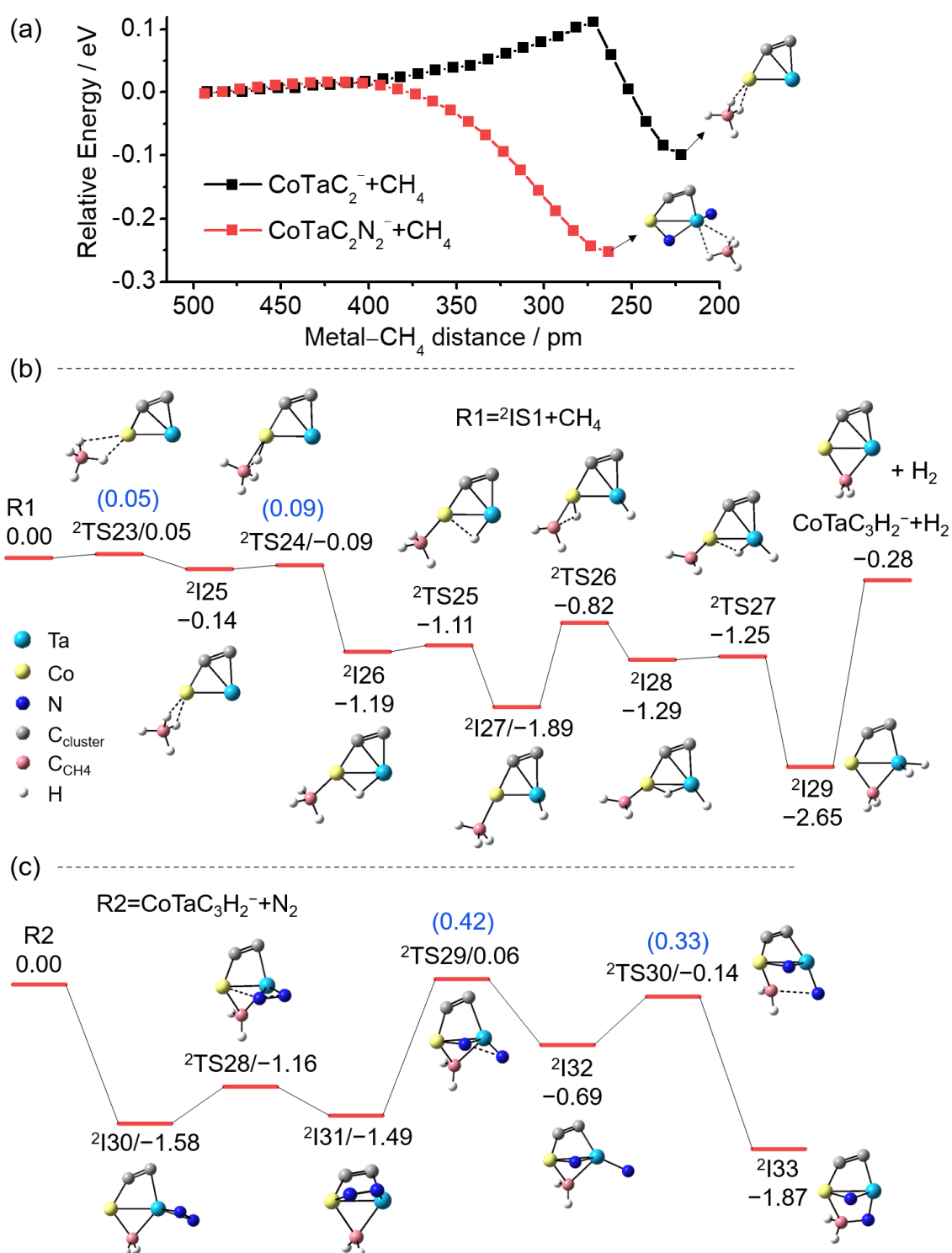## 3.3 A comparative study on exchanging the order to activate N₂ and CH₄

Fig. S10 (a) Relaxed potential energy curve scans for the approach of CH₄ to CoTaC₂⁻ and CoTaC₂N₂⁻. Potential energy profiles for (b) the activation of CH₄ by CoTaC₂⁻ to produce CoTaC₃H₂⁻ and (c) the further activation of N₂ by CoTaC₃H₂⁻. The zero-point vibration corrected energies with respect to the separated reactants are given in eV. Energies calculated at the RCCSD(T) level are shown in parentheses.

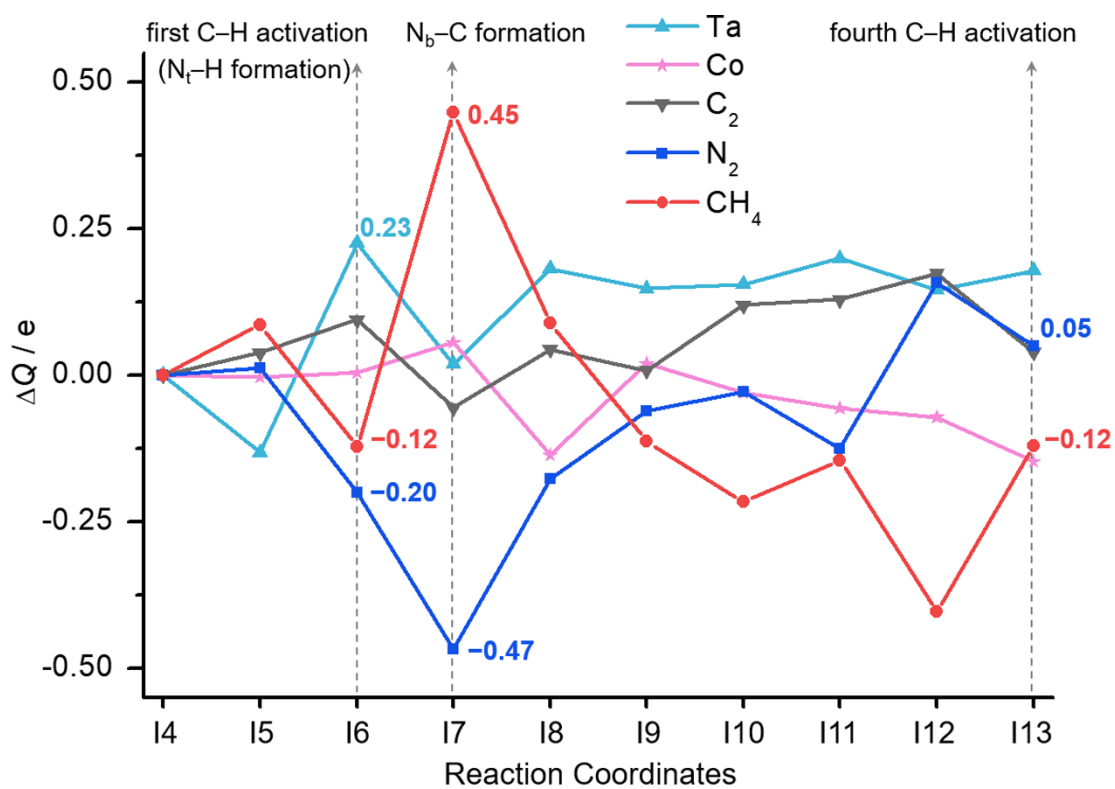## 3.4 Natural charge analysis and molecular orbital analysis

Fig. S11 Natural charge analysis for the activation of four C–H bonds of CH_4 by $CoTaC_2N_2^-$. The change of natural charges on metal atoms, two $C_{cluster}$ atoms, two N atoms, and CH_4 moiety is shown.
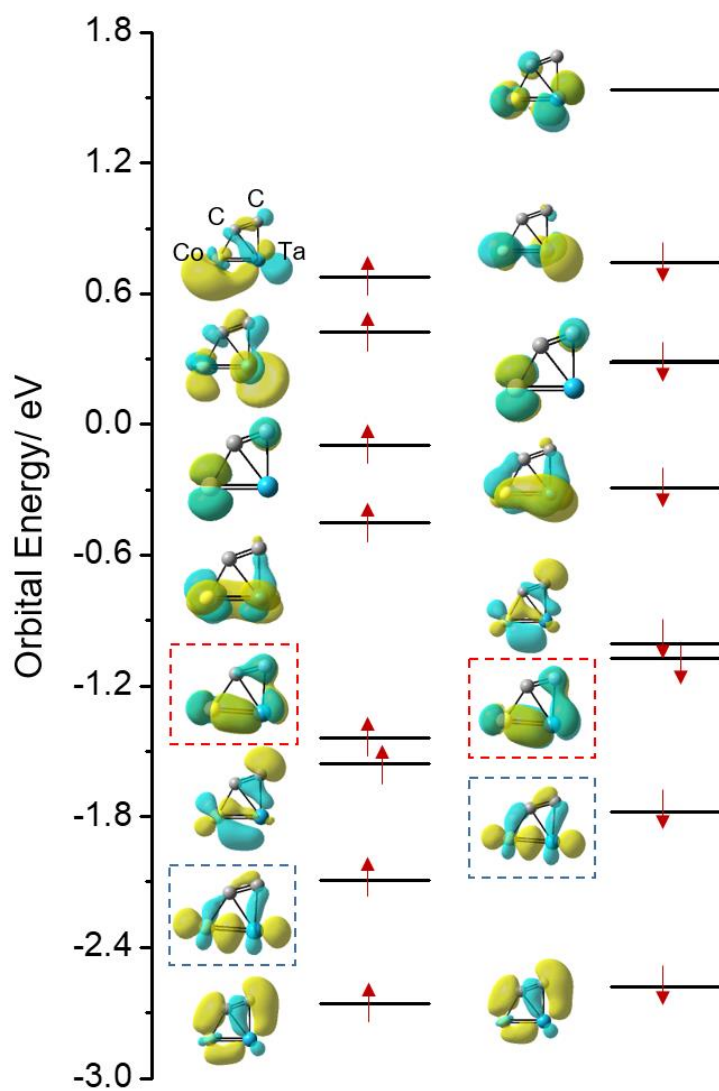
Fig. S12 Molecular orbital analysis of $CoTaC_2^-$. The up and down arrows denote α and β electrons. The two couples of d–d bonding orbitals between Co and Ta atoms indicates the presence of a Co–Ta double bond.

3.5 A comparative study on the reactivity of $FeTaC_2N_2^-$ toward CH_4
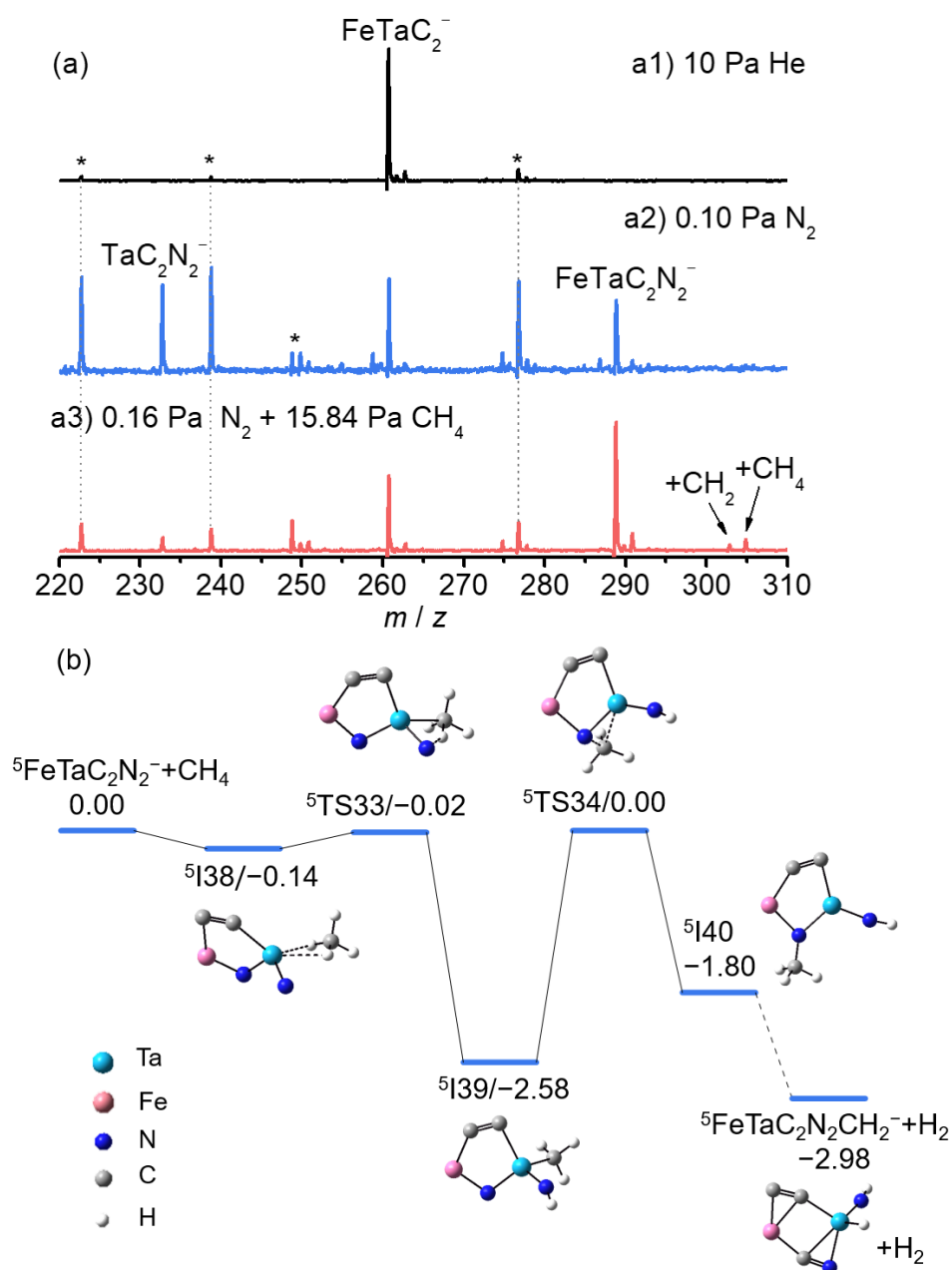

Fig. S13 TOF mass spectra for the reactions of mass-selected $FeTaC_2^-$ with (a1) 10 Pa He, (a2) 1% N_2 in 10 Pa He, and (a3) 1% N_2 in 16 Pa CH_4 in the ship-lock-type reactor for about 60 ms. The max gas pressures in the reactor are given. Peaks marked with asterisks are due to water impurities. (b) DFT-calculated potential energy profile for the reaction of $FeTaC_2N_2^-$ with CH_4. Only key TSs for $H_3C–H$ cleavage and N–C formation and the thermodynamics of H_2 elimination are shown for comparison with Co system.

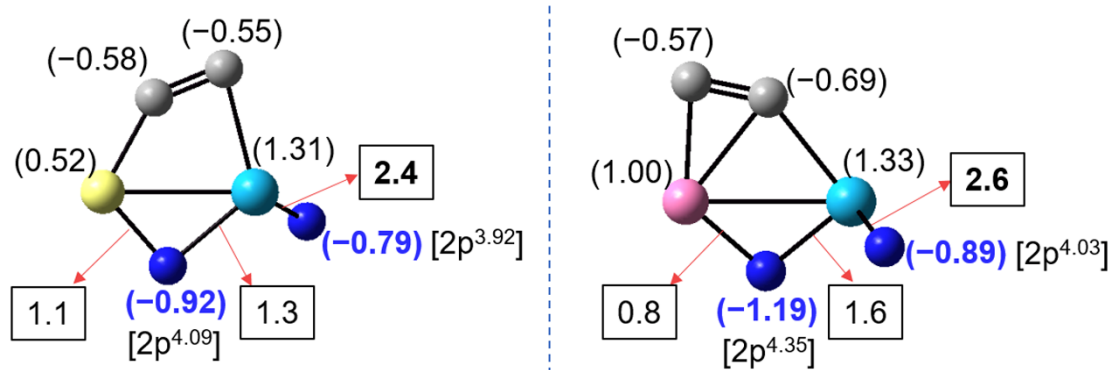**Fig. S14** The comparison of $CoTaC_2N_2^-$ (left) and $FeTaC_2N_2^-$ (right) in terms of natural charge (in parenthesis), electron occupancy on N_{2p} orbitals (in square brackets) and Wiberg bond index (in boxes).

4. References

1 Z. Yuan, Y.-X. Zhao, X.-N. Li and S.-G. He, *Int. J. Mass Spectrom.,* 2013, **354**, 105−112.

2 Z. Yuan, Z.-Y. Li, Z.-X. Zhou, Q.-Y. Liu, Y.-X. Zhao and S.-G. He, *J. Phys. Chem. C*, 2014, **118**, 14967−14976.

3 Y.-X. Zhao, Z.-Y. Li, Z. Yuan, X.-N. Li and S.-G. He, *Angew. Chem., Int. Ed.*, 2014, **53**, 9482−9486.

4 L.-H. Mou, Y. Li, Z.-Y. Li, Q.-Y. Liu, H. Chen and S.-G. He, *J. Am. Chem. Soc.*, 2021, **143**, 19224−19231.

5 G.-P. Wei, Q.-Y. Liu, Y. Ren and S.-G. He, *Rev. Sci. Instrum.*, 2021, **92**, 104104.

6 Q.-Y. Liu, L. Hu, Z.-Y. Li, C.-G. Ning, J.-B. Ma, H. Chen and S.-G. He, *J. Chem. Phys.* 2015, **142**, 164301.

7 M. J. Frisch, G. W. Trucks, H. B. Schlegel, G. E. Scuseria, M. A. Robb, J. R. Cheeseman, G. Scalmani, V. Barone, B. Mennucci, G. A. Petersson, H. Nakatsuji, M. Caricato, X. Li, H. P. Hratchian, A. F. Izmaylov, J. Bloino, G. Zheng, J. L. Sonnenberg, M. Hada, M. Ehara, K. Toyota, R. Fukuda, J. Hasegawa, M. Ishida, T. Nakajima, Y. Honda, O. Kitao, H. Nakai, T. Vreven, J. A. Montgomery, Jr., J. E. Peralta, F. Ogliaro, M. Bearpark, J. J. Heyd, E. Brothers, K. N. Kudin, V. N. Staroverov, R. Kobayashi, J. Normand, K. Raghavachari, A. Rendell, J. C. Burant, S. S. Iyengar, J. Tomasi, M. Cossi, N. Rega, J. M. Millam, M. Klene, J. E. Knox, J. B. Cross, V. Bakken, C. Adamo, J. Jaramillo, R. Gomperts, R. E. Stratmann, O. Yazyev, A. J. Austin, R. Cammi, C. Pomelli, J. W. Ochterski, R. L. Martin, K. Morokuma, K.,V. G. akrzewski, G. A. Voth, P. Salvador, J. J. Dannenberg, S. Dapprich, A. D. Daniels, O. Farkas, J. B. Foresman, J. V. Ortiz, J. Cioslowski and D. J. Fox, Gaussian 09 (Revision A.01), Gaussian, Inc., Wallingford CT, 2009.

8 J. M.Tao, J. P. Perdew, V. N. Staroverov and G. E. Scuseria, *Phys. Rev. Lett.*, 2003, **91**, 146401.

9 R. Krishnan, J. S. Binkley, R. Seeger and J. A. Pople, *J. Chem. Phys.*, 1980, **72**, 650−654.

10 F. Weigend and R. Ahlrichs, *Phys. Chem. Chem. Phys.*, 2005, **7**, 3297−3305.

11 B. P. Pritchard, D. Altarawy, B. Didier, T. D. Gibson and T. L. Windus, *J. Chem. Inf. Model.*, 2019, **59**, 4814−4820.

12 I. Berente and G. Naray-Szabo, *J. Phys. Chem. A*, 2006, **110**, 772−778.

13 C. Gonzalez and H. B. Schlegel, *J. Chem. Phys.*, 1989, **90**, 2154−2161.

14 C. Gonzalez and H. B. Schlegel, *J. Phys. Chem.*, 1990, **94**, 5523−5527.

15 E. D. Glendening, J. K. Badenhoop, A. E. Reed, J. E. Carpenter, J. A. Bohmann, C. M. Morales and F. Weinhold, NBO 5.9, Theoretical Chemistry Institute, University of Wisconsin, 2009.

16 T. Lu and F. W. Chen, *J. Comput. Chem.*, 2012, **33**, 580−592.

17 G. D. Purvis and R. J. Bartlett, *J. Chem. Phys.*, 1982, **76**, 1910−1918.

18 K. Raghavachari, G. W. Trucks, J. A. Pople and M. Head-Gordon, *Chem. Phys. Lett.*, 1989, **157**, 479−483.

19 J. D. Watts, J. Gauss and R. J. Bartlett, *J. Chem. Phys.*, 1993, **98,** 8718−8733.

20 P. J. Knowles, C. Hampel and H. J. Werner, *J. Chem. Phys.*, 1993, **99**, 5219−5227.

21 S. Guo, M. A. Waston, W. F. Hu, Q. M. Sun and G. K.-L. Chan, *J. Chem. Theory Comput.*, 2016, **12**, 1583–1591.

22 A. Y. Sokolva, S. Guo, E. Ronca and G. K-L. Chan, *J. Chem. Phys.*, 2017, **146**, 244102–244106.

23 H.-J. Werner, P. J. Knowles, R. Lindh, F. R. Manby, M. Schutz, P. Celani, T. Korona, A. Mitrushenkov, G. Rauhut, K. R. Shamasundar, T. B. Adler, R. D. Amos, A. Bernhardsson, A. Berning, D. L. Cooper, M. J. O. Deegan, A. J. Dobbyn, F. Eckert, E. Goll, C. Hampel, G. Hetzer, T. Hrenar, G. Knizia, C. Köppl, S. J. R. Lee, Y. Liu, A. W. Lloyd, R. A. Mata, A. J. May, S. J.

McNicholas, W. Meyer, M. E. Mura, A. Nicklaß, O. D. O'Neill, P. Palmieri, D. Peng, K. Pflüger, R. Pitzer, M. Reiher, U. Schumann, H. Stoll, A. J. Stone, R. Tarroni, T. Thorsteinsson, M. Wang and M. Welborn, Molpro, Version 2010.1. See http://www.molpro.net.

24 Q. M. Sun, T. C. Berkelbach, N. S. Blunt, G. H. Booth, S. Guo, Z. D. Li, J. Z. Liu, J. D. McClain, E. R. Sayfutyarova, S. Sharma, S. Wouters and G. K.-L. Chan, *Wires. Comput. Mol. Sci.*, 2018, **8**, e1340.

25 Q. M. Sun, J. Yang and G. K.-L. Chan, *Phys. Lett.*, 2017, **683**, 291−299.

26 G. K.-L. Chan and M. Head-Gordon, *J. Chem. Phys.*, 2002, **116**, 4462−4476.

27 J. J. Dorando, J. Hachmann and G. K.-L. Chan, *J. Chem. Phys.*, 2007, **127**, 084109.

28 E. Neuscamman, T. Yanai and G. K.-L. Chan, *J. Chem. Phys.*, 2010, **132**, 024106.

29 S. Sharma and G. K.-L. Chan, *J. Chem. Phys.*, 2012, **136**, 124121.

30 R. Olivares-Amaya, W. F. Hu, N. Nakatani, S. Sharma and G. K.-L. Chan, *J. Chem. Phys.*, 2015, **142**, 034102.

31 Y. H. Sun, H. Tang, K. J. Chen, L. R. Hu, J. N. Yao, S. Shaik and H. Chen, *J. Am. Chem. Soc.*, 2016, **138**, 3715−3730.

32 Z.-Y. Li, Y. Li, L.-H. Mou, J.-J. Chen, Q.-Y. Liu, S.-G. He and H. Chen, *J. Am. Chem. Soc.*, 2020, **142**, 10747−10754.

33 T. H. Dunning, *J. Chem. Phys.*, 1989, **90**, 1007−1023.

34 R. A. Kendall, T. H. Dunning and R. J. Harrison, *J. Chem. Phys.*, 1992, **96**, 6796−6806.

35 N. B. Balabanov and K. A. Peterson, *J. Chem. Phys.*, 2005, **123**, 064107.

36 D. Figgen, K. A. Peterson, M. Dolg and H. Stoll, *J. Chem. Phys.*, 2009, **130**, 164108.

37 T. Helgaker, W. Klopper, H. Koch and J. Noga, *J. Chem. Phys.*, 1997, **106**, 9639−9646.

38 A. J. Varandas, *J. Chem. Phys.*, 2007, **126**, 244105.

39 A. Halkier, T. Helgaker, P. Jorgensen, W. Klopper, H. Koch, J. Olsen and A. K. Wilson, *Chem. Phys. Lett.*, 1998, **286**, 243−252.

40 V. Mozhayskiy and A. I. Krylov, ezSpectrum v3.0. see http://iopenshell.usc.edu/downloads.

41 L.-J. Zhao, X.-L. Xu, H.-G. Xu, G. Feng and W.-J. Zheng, *New J. Chem.*, 2018, **42**, 16021−16026.

42 D. J. Tozer and N. C. Handy, *J. Chem. Phys.*, 1998, **109**, 10180−10189.

43 J. I. Steinfeld, J. S. Francisco and W. L. Hase, *Chemical Kinetics and Dynamics*, Prentice-Hall, 1999, pp. 231 and 313.

44 T. Beyer and D. F. Swinehart, *Commun. Acm.*, 1973, **16**, 379−379.

45 G. Gioumousis and D. P. Stevenson, *J. Chem. Phys.*, 1958, **29**, 294−299.

46 H.-F. Li, Z.-Y. Li, Q.-Y. Liu, X.-N. Li, Y.-X. Zhao and S.-G. He, *J. Phys. Chem. Lett.*, 2015, **6**, 2287−2291.

47 F. Buendia, M. R. Beltran, X. Zhang, G. Liu, A. Buytendyk and K. Bowen, *Phys. Chem. Chem. Phys.*, 2015, **17**, 28219−28227.

48 G. Liu, P. Poths, X. Zhang, Z. Zhu, M. Marshall, M. Blankenhorn, A. N. Alexandrova and K. H. Bowen, *J. Am. Chem. Soc.*, 2020, **142**, 7930−7936.

49 A. Sevy, D. M. Merriles, R. S. Wentz and M. D. Morse, *J. Chem. Phys.*, 2019, **151**, 024302.

50 Y. R. Luo, *Comprehensive Handbook of Chemical Bond Energies*, CRC Press, 2010.